LANGMUIR

pubs.acs.org/Langmuir Article

Physicochemical Properties of Monolayers of a Gemini Surfactant with a Minimal-Length Spacer

Srikant Kumar Singh, Alfred Yeboah, Wei Bu, Pan Sun, and Matthew F. Paige*



Cite This: Langmuir 2022, 38, 16004-16013



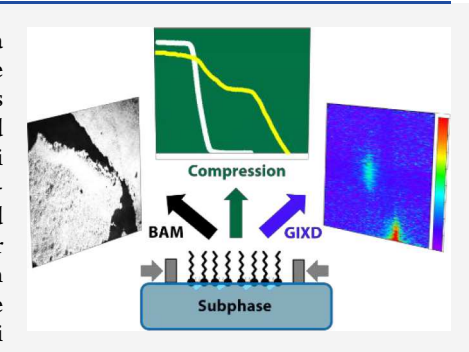
ACCESS

Metrics & More

Article Recommendations

Supporting Information

ABSTRACT: Fundamental physical chemical properties of monolayers formed from a new anionic gemini surfactant with a minimal-length (single-bond) spacer unit have been investigated at the air—water interface and compared with those of monolayers formed from affiliated comparator surfactants. The minimal spacer surfactant, dubbed C_{18} -0- C_{18} , exhibited strikingly different packing characteristics from an anionic gemini surfactant with a comparatively bulkier headgroup, including the formation of close-packed, crystalline films, and shared similar characteristics to simple fatty acid-based monolayers. Monolayers of C_{18} -0- C_{18} also exhibited good stability at the air—water interface and transferred with reasonable efficiency to solid substrates, although the film integrity was compromised during the transfer. Results from this work suggest that the single-bond spacer approach might be more broadly useful for designing gemini surfactants that pack efficiently into ordered monolayers.



1. INTRODUCTION

Gemini surfactants are an important class of dimeric surfaceactive reagents, and the variety of chemical structures to be found within this comparatively young class of compounds is already immense. $^{1-13}$ The seminal gemini surfactants reported by Zana et al. 14 were simple cationic species consisting of two headgroups and two aliphatic chains separated by a spacer; the original compounds were based upon quaternary ammonium ion headgroups and alkyl tails and were typically referred to as "m-s-m" surfactants with m and s reflecting the molecular length of the alkyl tail and spacer group, respectively. Since their original inception, a wide variety of gemini and geminilike surfactants have been synthesized and described in the literature and have been reviewed extensively. 1,4,15-22 These surfactants have found diverse applications, particularly in biomedical applications associated with drug delivery, in large part because of their low critical micelle concentrations and their ability to self-assemble into diverse and novel structures in aqueous solution.

Our research group and others have been investigating fundamental properties of surfactant aggregates (films and micelles) formed from a recently reported class of anionic gemini surfactants dubbed Ace(n)-m-Ace(n) (Scheme 1). First described by Wattebled et al., 6 these synthetically tractable compounds and their variants show excellent metal-chelating properties and pH response, 23,24 useful emulsification properties, and the ability to form stable monolayers at air—water and solid—air interfaces. Monolayer studies of these compounds are particularly useful as they provide direct information about the molecular packing of gemini surfactants in their aggregated states, and thus systematic structure—monolayer property studies can enable the correlation of film properties with the

underlying chemical structure of the surfactant. An important property of the Ace(n)-2-Ace(n) monolayers gleaned from our previous work is their inability to form close-packed, solid films at the air—water interface. While both n = 12 and 18 variants formed stable monolayers on water (Langmuir films), the resulting monolayers were expanded and the liquid phase for all conditions was explored, as evidenced by surface pressure area $(\pi - A)$ isotherm measurements and grazing incidence Xray diffraction (GIXD) studies. The working hypothesis for this effect, suggested by X-ray reflectivity (XR) measurements and accompanying electron density distribution modeling, was that the sterically bulky headgroups impeded the ability of the surfactant to close-pack and that the conformationally flexible headgroups tended to flatten on the air-water interface with a net effect of yielding liquid-phase films regardless of the extent of film compression.

We have chosen to explore the importance of surfactant headgroup structure on monolayer film properties by studying a structural variant of the original compound, a so-called "gemini without a spacer group" as described by Villa et al.²⁵ In these compounds, the spacer between two nominal anionic headgroups has been replaced by the shortest possible spacer, a single covalent bond between the carbon atoms in the headgroup. In broad terms, the length and chemical

Received: September 7, 2022 Revised: November 24, 2022 Published: December 15, 2022





Scheme 1. Chemical Structures of (A) C₁₈-0-C₁₈, (B) Ace(18)-2-Ace(18), and (C) Stearic Acid

composition of the spacer appears to be the predominant chemical structural factor regulating critical micelle concentrations (CMCs) in many gemini systems; the alkyl tail length alone appears to be minimally important. 12,26-28 Thus, control over the spacer should provide significant control over aggregation and packing behavior in condensed films. In addition to the minimal spacer, the headgroups in these compounds also differ from Wattebled's original compounds which contained tertiary amines to aid in metal chelation, but they nonetheless retain significant structural similarities. We hypothesize that members of this group will form stable monolayers at the air-water interface, as per Ace(18)-2-Ace(18), but because of the more compact nature of the headgroup, close-packing of the species will be possible. To this end, we have synthesized an 18-carbon-long tailgroup molecule, the same tailgroup length as Ace(18)-2-Ace(18), with a minimal spacer group (Scheme 1). We herein referred to the new compound as C₁₈-0-C₁₈. Variants of this compound have been reported in detail elsewhere by Kunieda et al.^{29,30} and Aramaki et al.31 The central theme of this report is an investigation of the properties of C₁₈-0-C₁₈ Langmuir monolayers using a variety of monolayer characterization methods and a discussion of results in the context of other monomeric fatty acids or dimeric Ace(n)-2-Ace(n) compounds with equivalent/similar structural features (for example, chain length, n = 18 for stearic acid; Scheme 1) that have been previously reported in the literature.

2. EXPERIMENTAL SECTION

2.1. Synthesis and Characterization of C_{18} -O- C_{18} . Reagents and solvents were purchased from Sigma-Aldrich and were used as received without further purification. Solvents were ACS grade or

better. The chemical synthesis was adapted from ref 25 with additional details provided in the SI. In brief, cis-1,2,3,6-tetrahydrophtalic anhydride and 1-octadecanol were mixed in the presence of p-toluenesulfonic acid (PTSA, 20% by weight of the anhydride) as the acidic catalyst under conventional reflux at 110 °C in 250 mL of toluene for ~16 h (Scheme 2 shown below; R = $C_{18}H_{37}$). Product (2) was purified by recrystallization from 80 vol % ethanol (yield = 79%).

Scheme 2. Reaction Scheme for the Synthesis of Surfactants of Interest

The second step involved adding KMnO₄ to purified product (2) in an ice bath which was stirred overnight (\sim 18 h). Resulting product (3) was purified by recrystallization from *n*-hexane/ethyl acetate 9:1 (yield \sim 64%), and the chemical structure of the product was confirmed by ¹H NMR and ESI-mass spectrometry. Qualitative powder X-ray diffraction analysis confirmed the bulk crystallinity of the sample and was also used to determine the consistency between

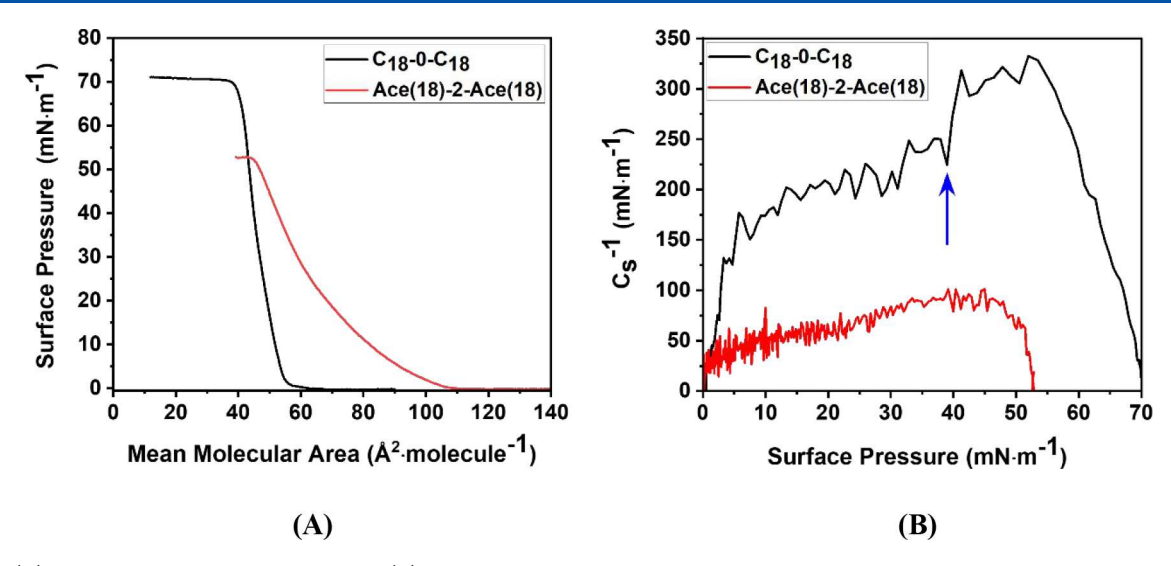


Figure 1. (A) Isotherms of surfactants of interest (B) with their corresponding compressibility plots.

different batches synthesized. Characterization data have been appended in the Supporting Information.

2.2. Film Preparation and Characterization. Langmuir films were prepared on a Langmuir trough (KSV Nima; Biolin KSV) equipped with a Wilhelmy plate balance and a pure water (Barnstead, resistivity = 17.2 $M\Omega \cdot cm^{-1}$) subphase. The trough was operated in a symmetric compression (or expansion) mode, and surface pressure was monitored using a filter paper plate. The water surface was cleaned by suction thoroughly before each experiment to ensure a clean subphase surface. Thereafter, 100 µL aliquots of the surfactant solution (C₁₈-0-C₁₈ in chloroform, 1.0 mM) were spread onto the subphase surface using a Hamilton syringe, and the film was allowed to equilibrate for ~15 min (for solvent evaporation) prior to measurements. Films were compressed/expanded at a rate of 20 mm²· min⁻¹ (approximately 5.0 Å² molecules⋅min⁻¹). Several replicate isotherms were performed for each system to ensure reproducibility. Surface potential measurements at the air-water interface were performed with a calibrated, vibrating plate probe (KSV Instruments) mounted on the trough. The surface potential probe was calibrated with a known DC voltage before beginning experiments.

Mechanical properties of the film were determined using the same trough system as described above. In the kinetic isotherm measurements $(\pi-t)$, the same general procedure as used to obtain a $\pi-A$ isotherm was adopted, except that the film was held at a target surface pressure of $\pi=30~{\rm mN\cdot m^{-1}}$ by the continuous adjustment of the barrier position while the film area was recorded as a function of time. For hysteresis experiments, either the range of surface pressure $(\pi_{\rm min}=0~{\rm mN\cdot m^{-1}}$ to $\pi_{\rm max}=40~{\rm mN\cdot m^{-1}})$ or the mean molecular area $(A_{\rm max}=59.4~{\rm Å^2\cdot molecule^{-1}})$ was varied to observe the monolayer response to repeated compression—expression cycles.

Brewster angle microscopy (BAM) imaging was conducted on an UltraBAM microscope (KSV Biolin) equipped with a 658 nm illumination laser and a camera operating at an acquisition rate of 20 frames \cdot s⁻¹.

GIXD and XR measurements were conducted on the liquid surface scattering spectrometer of sector 15-ID-C (NSF's ChemMatCARS) at the Advanced Photon Source (Argonne National Laboratories). Films were prepared on a Langmuir trough equipped with a single movable barrier, and the trough was encased in a sealed chamber mounted on a vibration isolation pad. The liquid footprint inside the trough had dimensions of 42.0 cm (length) \times 8.9 cm (width) \times 0.7 cm (depth). Surfactant solution was spread onto a clean water surface in the trough, as described in the preceding section, and the chamber was purged with helium to minimize X-ray beam scattering by air and to minimize potential damage to the film caused by the incident beam. For the GIXD measurements, a monochromatic beam of X-rays with

an energy of 10.0 keV and an approximate size of 0.1 mm \times 2.0 mm was directed onto the subphase surface at a selected incident angle (\sim 0.1°), and diffracted X-rays were collected on a Pilatus 200 K X-ray detector (Dectris). For XR, the beam size and incident angle were adjusted for different q_z values. The X-ray beam intensity was adjusted to ensure that no damage was being caused to the film during the time course of the experiments. The X-ray diffraction intensity was measured as a function of in-plane (q_{xy}) and out-of-plane (q_z) scattering vectors, and the reflected intensity was measured as a function of out-of-plane scattering (q_z) .

3. RESULTS AND DISCUSSION

3.1. Compression Isotherms and Surface Potential. π –A isotherms for monolayer films of C_{18} -0- C_{18} and Ace(18)-2-Ace(18) at the air—water interface are shown in Figure 1(A). Limiting mean molecular areas for the films were estimated by fitting a straight line to the region right before the film collapse and extending it to the abscissa. To reveal any phase transitions not discernible in the isotherms, monolayer compressibility plots $(C_s^{-1} = -A(d\pi/dA)_T \text{ vs } \pi)$ were calculated and are reported in Figure 1(B). Quantitative data extracted from the isotherms are specified in Table 1.

Table 1. Summary Isotherm Data for C₁₈-0-C₁₈ and Ace(18)-2-Ace(18) Monolayer Films^a

composition	A_0 (Å ²)	$\pi_{\rm c}~({\rm mN}{\cdot}{\rm m}^{-1})$	$C_{\rm s~max}^{-1}$ (mN·m ⁻¹)
C_{18} -0- C_{18}	50.8 ± 0.3	70.3 ± 0.8	332.5 ± 0.5
Ace(18)-2-Ace(18)	76.1 ± 0.1	53.5 ± 0.5	101.1 ± 0.2

^aMeasurements were carried out in triplicate, and reported values are means with standard deviations for uncertainty ranges.

The overall shape of the C_{18} -0- C_{18} isotherm resembles typical single-chain fatty acids such as behenic acid and stearic acid with a similar collapse pressure. The limiting area per molecule for C_{18} -0- C_{18} was found to be \sim 51 Ų, which is approximately double the limiting area typically observed for other single-chain fatty acids, which exhibit close packing in compressed films (e.g., stearic acid, 20.7 Ų). If C_{18} -0- C_{18} is viewed as a crude dimer of two fatty acids with negligible flexibility within the headgroup, then the limiting area is consistent with efficient close packing of the surfactant. The isotherm for Ace(18)-2-Ace(18) is significantly expanded in

comparison with C_{18} -0- C_{18} as evidenced by a higher limiting area of Ace(18)-2-Ace(18), as is expected for the liquid-phase monolayer. The difference in the two monolayers is also apparent from the quite different collapse pressures (π_c). The collapse pressure is often correlated with the collapse mechanism of the monolayer, ³⁵ with rigid monolayers typically collapsing at higher surface pressures than fluid films at the air—water interface. Thus, the higher collapse pressure for C_{18} -0- C_{18} films highlights its comparative rigidity compared with the fluid Ace(18)-2-Ace(18) monolayer.

In addition to the raw isotherms alone, compressibility plots for the C_{18} -0- C_{18} and Ace(18)-2-Ace(18) monolayers provide additional insight into their nature. Figure 1(B) and Table 1 show that the Ace(18)-2-Ace(18) films are, as expected, more compressible than C_{18} -0- C_{18} with the maximum of the compressibility modulus plot $(C_s^{-1}_{\max})$ point of minimum fluidity of the film) being ~101.1 and ~332.5 mN·m⁻¹ for both of the films, respectively. The greater compressibility of Ace(18)-2-Ace(18) can be attributed primarily to its liquid nature but also in part to its previously reported headgroup flexibility, whereas the maximum values for C_{18} -0- C_{18} are consistent with values for solid-like films.³⁶ Careful inspection of the compressibility plot for C₁₈-0-C₁₈ reveals an inflection point (marked by a blue arrow) at ~40 mN·m⁻¹ suggesting a phase transition. Again, there are striking parallels between this system and simple monomeric fatty acids, in which the tilted condensed to untilted condensed phase transition is seen at similar surface pressures and temperatures. 32,33,37-39

To further assess molecular orientation at the interface, the surface potential was measured as a function of film area (ΔV – A) for pure C_{18} -0- C_{18} (Figure 2). Using a simple, minimal

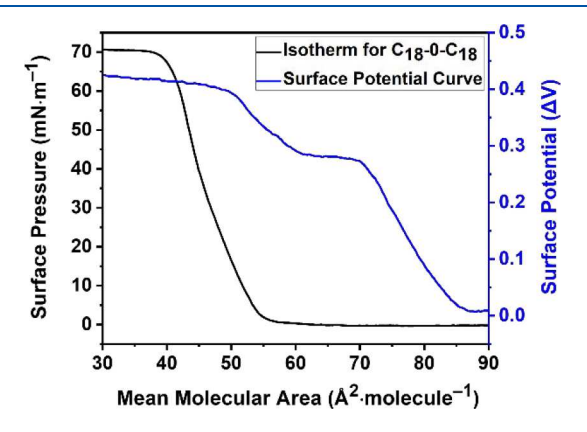


Figure 2. Surface potential versus mean molecular area for C_{18} -0- C_{18} . The corresponding compression isotherm is included for comparison purposes.

Helmholtz model (e.g., $\mu_{\perp} = \epsilon_0 \Delta V A$, where ϵ_0 is vacuum permittivity, ΔV is surface potential after appropriate zeroing against pure water, and A is mean molecular area) allows a rudimentary correlation of the molecular dipole moment, which we assume here to run along the length of C_{18} -0- C_{18} toward the surfactant headgroup, with film structure during compression. The surface potential broadly increased with film compression at large MMA, consistent with the orientation of the C_{18} -0- C_{18} dipole moment toward the normal as a function of compression. Two well-defined plateaus in surface potential were observed, one starting just prior to the film collapse pressure, as can be expected, and a second at $\pi \approx 40$ mN·m⁻¹, which correlates with the discontinuity observed in the

compressibility curve. We take the latter as cumulative evidence for a first-order phase transition at this surface pressure. Furthermore, the significant increase in the dipole moment after the transition is again consistent with a collective change in molecular tilt toward the surface normal. Calculating changes in molecular tilt from the dipole data is fraught with potential errors but can be done with precision using diffraction data (vide infra).

3.2. Hysteresis and Film Stability. To qualitatively assess the stability of C₁₈-0-C₁₈ monolayers at the air-water interface, monolayer film hysteresis (i.e., how well the monolayer respreads after compression) was assessed by conducting a series of compression-expansion cycles of the monolayer. These measurements provide qualitative information on monolayer reorganization and/or irreversible desorption, with the results shown in Figure 3(A) and (B). For the hysteresis experiment, the monolayers were compressed up to a target surface pressure of $\pi_{\text{max}} = 40 \text{ mN} \cdot \text{m}^{-1}$, and then after a time delay of 5 s, they were expanded until reaching a target surface pressure of $\pi_{\min} = 0 \text{ mN} \cdot \text{m}^{-1}$. When the monolayer was expanded the first time (viz. E1), there was a steep drop in the surface pressure to $\pi = 0 \text{ mN} \cdot \text{m}^{-1}$, and on recompression (C2), the surface pressure increases rapidly to π_{max} . While the largest change in isotherms was observed with the first compression-expansion cycle, additional but smaller changes toward a lower mean molecular area were observed between successive cycles. To confirm this observation, the experiment was repeated with a narrower range of barrier compression shown in Figure 3(B) (i.e., keeping the target mean molecular area $A_{\text{max}} = 59.4 \text{ Å}^2 \cdot \text{molecule}^{-1}$ and the return target $A_{\text{min}} =$ 58.2 Å²·molecule⁻¹). All other parameters (such as the delay time between consecutive compression-expansion cycles = 5 s) were kept the same to allow for the direct comparison of results. We note that in all cases there was hysteresis between the compression and expansion curves within the same cycle, which can reasonably be attributed to the kinetics of respreading of the compressed film.

The most plausible explanation for the film hysteresis between successive cycles is that the monolayer is successively losing small quantities of film material into the subphase, which appears as a progressive shift toward a lower film area with successive compression—expansion cycles. Minimal loss of film material with each cycle is a common behavior for many stable monolayers. For the case of C_{18} -0- C_{18} , the shift in the molecular area after five cycles was <0.25%, indicating that the monolayer is very stable, very similar to systems involving polpypeptide or stearic acid mixtures with modest mean molecular changes. There were comparable (or smaller) shifts in molecular area with more cycles (data not shown) but no substantial difference other than that shown above.

This agrees well with an independent isotherm experiment in which the monolayer was compressed until a target ($\pi \approx 30 \, \mathrm{mN \cdot m^{-1}}$) and then held for a period of approximately 2 h to observe the monolayer response over time. Figure 3(C) presents the mean molecular area—time (A–t) decay curves normalized to A/A_0 for C_{18} -0- C_{18} and Ace(18)-2-Ace(18) for comparison, where A_0 is the mean molecular area reached at time t=0. The relaxation behavior indicates that both monolayers have different relaxation characteristics in both initial and later stages; qualitative fitting of the curves with multiexponential decays suggests a complex mechanism of film relaxation. Most importantly, the C_{18} -0- C_{18} monolayer again exhibits a very stable characteristic with negligible area loss

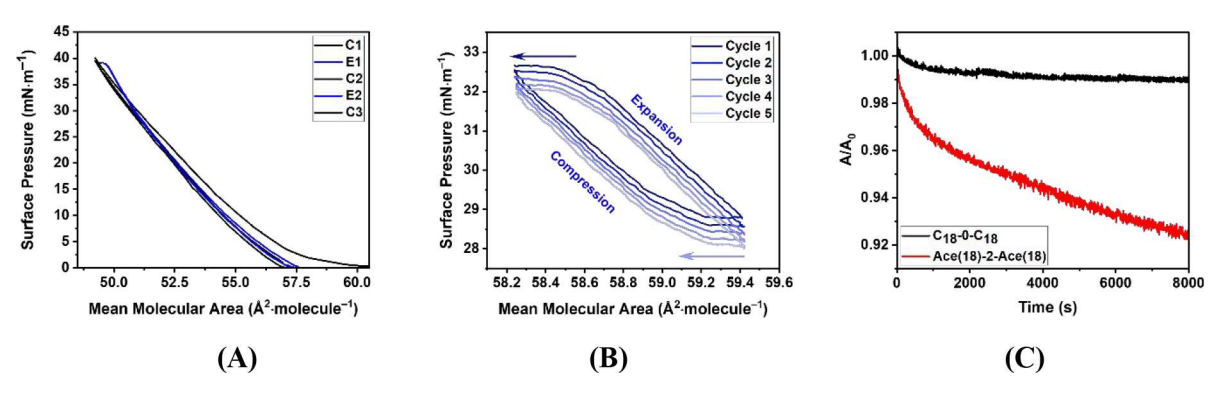


Figure 3. Hysteresis plots (surface pressure versus mean molecular area) for C_{18} -0- C_{18} highlighting different data ranges. (A) Measurements with film area in the range of 50–60 Å²-molecule⁻¹. In the legend, C# indicates a compression cycle and E# indicates an expansion cycle. (B) Measurements with film area in the range of 59.4–58.2 Å²-molecule⁻¹. The arrows indicate the direction of shift in the hysteresis loops. (C) Plot showing the normalized film area as a function of time for monolayer films held at $\pi = 30 \text{ mN·m}^{-1}$.

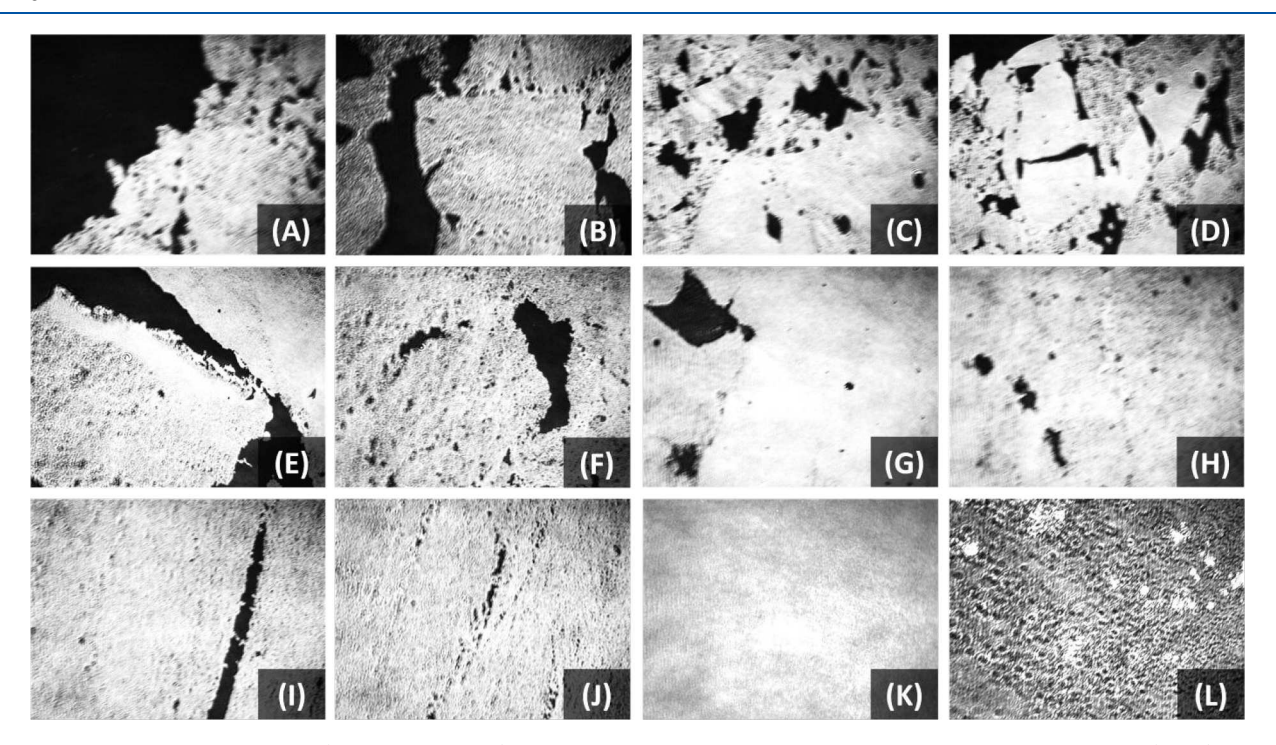


Figure 4. Representative BAM images (696 μ m × 520 μ m) for pure C₁₈-0-C₁₈ monolayer films as a function of surface pressures (A–D) 0–5 mN·m⁻¹, (E–H) 5–15 mN·m⁻¹, and (I–K) 15–30 mN·m⁻¹ and beyond until collapse. (L) At and around collapse. Images were collected at $T = 21 \pm 1$ °C.

(\sim 0.02%) during the relaxation period. In contrast, the Ace(18)-2-Ace(18) film loses area rapidly with an area loss of \sim 0.08% within a similar time frame. The small amount of barrier compression needed to hold the surface pressure at $\pi = 30 \text{ mN} \cdot \text{m}^{-1}$ for C_{18} -0- C_{18} is comparable to that of a stearic acid monolayer under similar conditions, ³⁸ which also forms a solid-like film at the air—water interface.

3.3. BAM Measurements. To characterize micrometer-scale film morphology at the air—water interface, BAM images for monolayer films were collected over a range of surface pressures, with representative images shown in Figure 4. In the images, the low reflectivity (dark) regions in the background are ascribed to water, based on the difference in the reflective indices of the subphase and the monolayer. In general, C_{18} -0- C_{18} monolayers contained large, highly reflective regions throughout the entire range of surface pressures measured. Bright patches of film spanning hundreds of micrometers were

detectable at surface pressures of as low as $\pi = 0-5 \text{ mN}\cdot\text{m}^{-1}$, as shown in Figure 4(A)-(D). At the lowest pressure ranges, irregular void regions were frequently observed within the bright patches. As the film was further compressed ($\pi = 5-15$ $mN \cdot m^{-1}$), the dark irregular voids between the patches became smaller and smaller until the film became increasingly uniform (Figure 4(E)-(H)). Throughout the compression experiment, cracks and apparent ridges were visible in the film, which suggested a significant degree of crystallinity in the films. The cracks (seen Figure 4(I) and (J)) became increasingly rare as the film was further compressed, and by $\pi \approx 30 \text{ mN} \cdot \text{m}^{-1}$, the films were essentially homogeneous and highly reflective, suggesting the formation of a uniform, packed film (within the resolution limit of the microscope), which unfortunately meant that changes to the film structure that accompanied the phase transition at $\pi \approx 40 \text{ mN} \cdot \text{m}^{-1}$ could not be further elucidated with BAM. At and above the collapse of the film (Figure 4(L)),

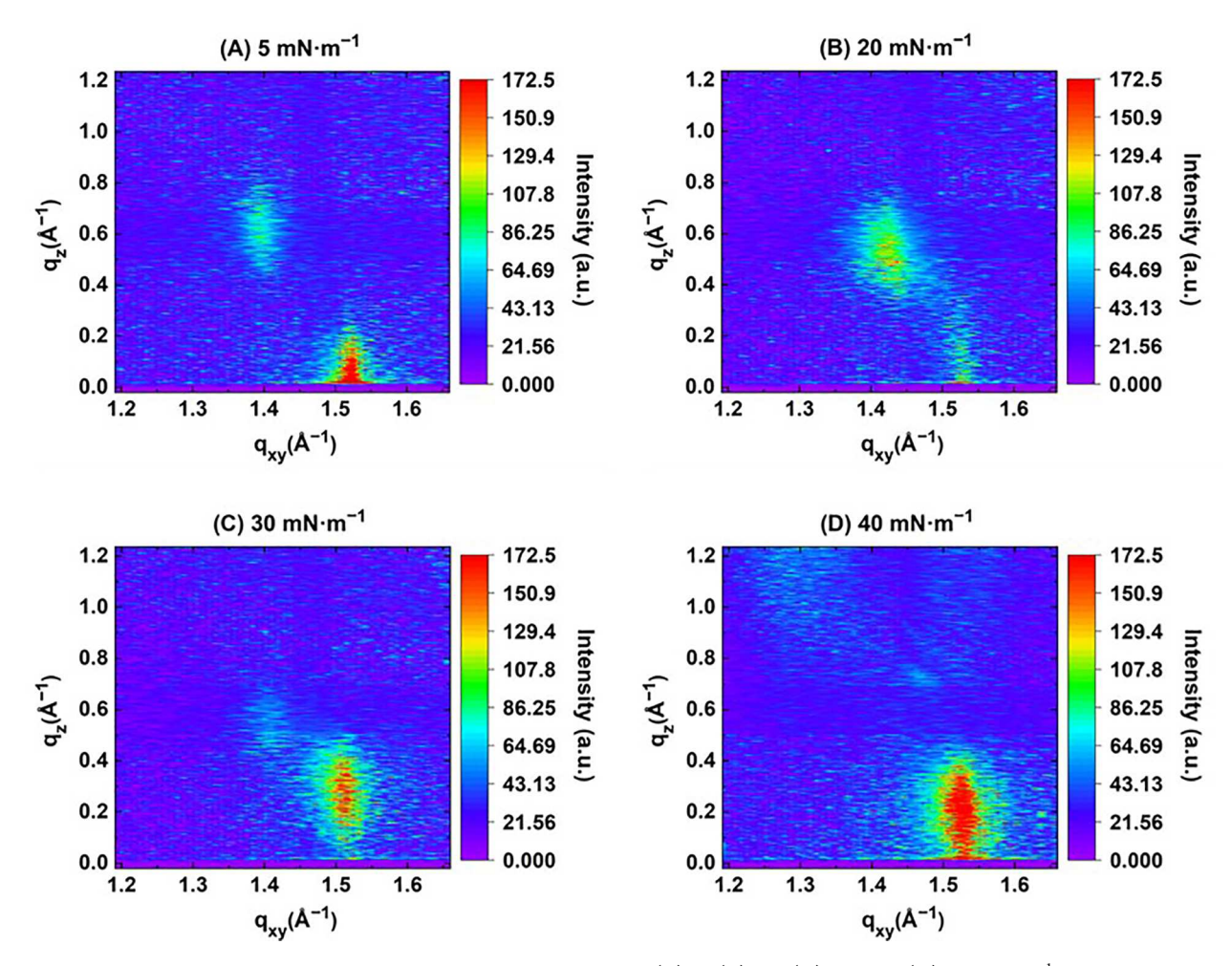


Figure 5. GIXD contour plots for C_{18} -0- C_{18} at different surface pressures: (A) 5, (B) 20, (C) 30, and (D) 40 mN·m⁻¹.

an abundance of small structures was detected, presumably corresponding to complex aggregates that formed after film collapse.

From a comparison point of view, C_{18} -0- C_{18} monolayers were quite different from those observed for Ace(18)-2-Ace(18), which were generally featureless and minimally reflective, except for occasional micrometer-sized amorphous domains. (See the Supporting Information for an example.) C_{18} -0- C_{18} monolayers more closely resembled those reported for single-chain (crystalline) fatty acid and alcohol monolayers with similar chain lengths, for example, 1-hexadecanol, stearic acid, stearyl palmitate, ethyl behenate, and oleanolic acid monolayers which tend to form similar, continuous films with occasional cracks at the air—water interface.

We have also attempted to characterize the nanometer-scale morphology of deposited (Langmuir–Blodgett, LB) C_{18} -0- C_{18} monolayers. Previous attempts at the LB monolayer deposition of Ace(12)-2-Ace(12) and its longer-chain analogue onto various solid substrates have generally resulted in either poor transfer (at low surface pressures) or in the deposition of multilayer aggregates, typically with transfer ratios that were much larger than one (unpublished data; similar observations have been published for Fe³⁺-enriched subphases⁴⁹), likely because of the fluid nature of the films. Intriguingly, C_{18} -0- C_{18} films could be deposited onto glass substrates over a range of surface pressures with transfer ratios of \sim 1, indicating efficient monolayer transfer. AFM height mode images of samples

deposited at $\pi = 30 \text{ mN} \cdot \text{m}^{-1}$ (Supporting Information, Figure S5) revealed patches of deposited material across the substrate. However, cross-sectional analysis of AFM height images for films deposited indicated the formation of aggregates (typical heights ~ 5 nm, with occasional features at ~ 10 nm), suggesting that the films become unstable during the deposition and drying process.

3.4. Grazing Incidence X-ray Diffraction and X-ray Reflectivity. As an ultimate assessment of film crystallinity and crystallographic film structure, monolayer films were measured using GIXD at the air—water interface. Monolayer films were found to diffract strongly at all surface pressures, indicating that C_{18} -0- C_{18} indeed formed crystalline monolayers. Figure 5(A)-(D) shows diffraction patterns for the monolayers at a selection of different surface pressures. To the best of our knowledge, there are very few if any reports of gemini surfactants that definitively form crystalline monolayers at the air—water interface, albeit this may be because of the relative scarcity of GIXD facilities needed to assess this rather than a general chemical property of these compounds. Nonetheless, this is an important result and confirms the observations above.

The ability to form crystalline monolayers for this general class of geminis has been significantly impacted by the minimal spacer headgroup; neither Ace(12)-2-Ace(12)⁵⁰ nor its n = 18 counterpart formed diffracting monolayers at the air—water interface (Figure 6), whereas the minimal spacer headgroup

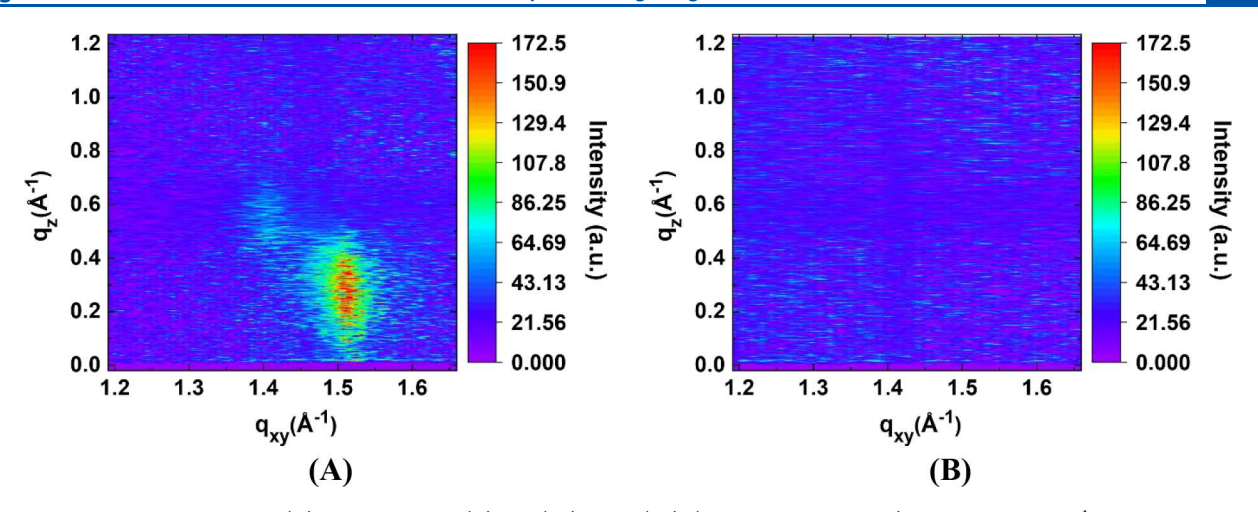


Figure 6. GIXD contour plots for (A) C_{18} -0- C_{18} and (B) Ace(18)-2-Ace(18) (modified from ref 51) at $\pi = 30 \text{ mN} \cdot \text{m}^{-1}$.

Table 2. Summary GIXD Data for Pure C₁₈-0-C₁₈ Monolayer Films at Different Surface Pressures

$\pi \text{ (mN·m}^{-1}\text{)}$	indexed peaks	q_{xy} maxima $(\mathring{\mathrm{A}}^{-1})$	fwhm	d spacing (Å ± 0.01)	unit cell area/chain $(\mathring{A}^2 \pm 0.1)$	coherence length $(\mathring{A} \pm 10)$	$\begin{array}{c} q_z \text{ maxima} \\ (\text{Å}^{-1} \pm 0.01) \end{array}$	tilt angle (deg) and direction
5	[1, 1]	1.40	0.06	4.50	22.1	156.3	0.63	28.3, NN
	[0, 2]	1.52	0.05	4.13			0	
20	[1, 1]	1.42	0.08	4.42	21.6	94.5	0.55	24.4, NN
	[0, 2]	1.52	0.07	4.13			0	
30	[1, 1]	1.51	0.07	4.16	21.9	93.3	0.53	20.7, NNN
	[0, 2]	1.41	0.10	4.46			0.54	
40	all	1.52	0.07	4.12	19.6	99.7	0	0

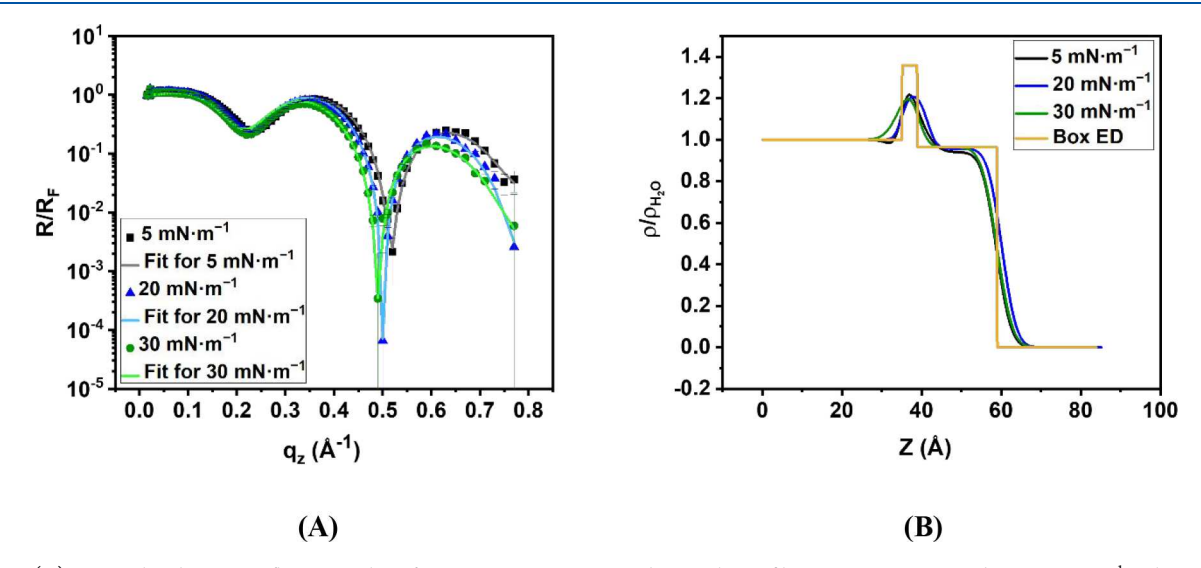


Figure 7. (A) Normalized X-ray reflectivity plots for pure C_{18} -0- C_{18} , mixed monolayer films at $\pi = 5$, 20, and 30.0 mN·m⁻¹. The points are experimental values while the solid curve is the fit. (B) Corresponding normalized electron density profiles for the data in part (A).

compound and simple fatty acid analogues diffract well, highlighting the crucial nature of this group in terms of ability to pack into crystalline lattices.

GIXD patterns at $\pi = 5 \text{ mN·m}^{-1}$ consisted of two Bragg peaks, the first at $q_{xy} = 1.39 \pm 0.02 \text{ Å}^{-1} (q_z = 0.63 \text{ Å}^{-1})$ and the second peak at $q_{xy} = 1.52 \pm 0.01 \text{ Å}^{-1} (q_z = 0 \text{ Å}^{-1})$, corresponding to a centered rectangular lattice with unit cell dimensions of a = 5.4 Å and b = 8.3 Å and area of 44.2 Å², which contains two hydrocarbon chains (22.1 Å² per alkyl chain). Bragg rods of the degenerate reflections ([1, 1], [1, 1]) are centered at $q_z \ge 0 \text{ Å}^{-1}$, whereas that of the nondegenerate reflection ([0, 2]) is at $q_z = 0 \text{ Å}^{-1}$, so the peak at lower q_{xy}

corresponds to the [1,1] peaks whereas the one at higher q_{xy} corresponds to the [0,2] peaks. This is typical for a tilt of the C_{18} -0- C_{18} alkyl chains in the nearest-neighbor (NN) direction. The two Bragg peaks were fitted to obtain d spacings of 4.5 Å for the [1,1] peaks and 4.1 Å for the [0,2] peaks (Table 2). Furthermore, a chain tilt angle of 28.3° was determined from the Bragg rod analysis, along with a coherence length of ~ 156.2 Å (calculated from the Scherrer equation 53 after deconvolution from instrumental broadening).

As the monolayers were compressed, diffraction patterns shifted to less distorted lattices and to lower molecular tilt angles. The diffraction intensity of the peak at $q_{xy} \approx 1.5 \text{ Å}^{-1}$

generally increased with compression. Changes in diffraction patterns were minimal at lower surface pressures but changed more substantially at higher pressures. Crystallographic data for the system response to compression is summarized in Table 2. Data for some intermediate surface pressures (π = 10 and 35 mN·m⁻¹) with similar crystallographic features to the ones specified in Table 2 (and Figure 5) have been added to the Supporting Information.

In brief, crystallographic properties at low surface pressures were all comparable until the film had been compressed to $\pi=30~\text{mN/m}$, at which point the Bragg rod maxima at $q_{xy}\approx1.5~\text{Å}^{-1}$ had shifted out of plane $(q_z>0)$, corresponding to a centered rectangular lattice $(a=5.3~\text{Å},b=8.3~\text{Å},\text{ area of }21.9~\text{Å}^2$ per alkyl chain) and a tilt (reduced in comparison to the lower film pressures) in the next-nearest neighbor (NNN) direction. A complex diffraction pattern intermediate between the low- and high-pressure patterns was observed at $\pi=35~\text{mN·m}^{-1}$ (Supporting Information). The precise lattice assignment for this pattern was ambiguous, and we qualitatively view this as a transitional structure that exists just before the hexagonal lattice.

At $\pi=40~{\rm mN\cdot m^{-1}}$, the highest pressure measured, a single diffraction peak was observed, which is closest in resemblance to a hexagonal lattice of untilted chains. The change in lattice arrangement (along with the reduction in molecular tilt) provides additional direct evidence of the phase transition mentioned in the description of the isotherm data. Similar transitions in crystallographic structure occur in the case of arachidic acid⁵⁴ at $\pi=30~{\rm mN\cdot m^{-1}}$, which is also correlated to a clear transition in its isotherm.³⁷

XR measurements were conducted for the monolayers at different surface pressures and are reported along with their corresponding normalized electron density profiles and model fits in Figure 7. Noticeable variations among the three curves in Figure 7(A) can be observed, but the experimental points contained substantial experimental uncertainties, particularly at higher q_z ($q_z > 0.35 \text{ Å}^{-1}$). To obtain information about the thickness of monolayers, the reflectivity was modeled using the software $Stochfit^{55}$ using a simple two-box model: one for the headgroup region and one for the tail region (two alkyl chains). During the refinement and model fitting, the subphase roughness was unlinked. Results are summarized in Table 3. At

Table 3. XR Parameters for C_{18} -0- C_{18} at Different Surface Pressures

surface pressure $(mN \cdot m^{-1})$	layer	length (Å)	electron density $(ho/ ho_{ m sub})$
5	tail	20.7 ± 0.3	0.94 ± 0.01
	head	3.1 ± 0.3	1.5 ± 0.1
20	tail	18.7 ± 0.4	0.96 ± 0.01
	head	6.5 ± 0.8	1.2 ± 0.03
30	tail	21.0 ± 0.3	0.96 ± 0.01
	head	3.9 ± 1	1.4 ± 0.1

higher surface pressures, the experimental data could not be fit by a variety of models; the reason for this remains unclear, but because of this, we report data only from low surface pressures.

For the range of surface pressures that could be appropriately analyzed ($\pi = 5$, 20, and 30 mN·m⁻¹), the fits for C₁₈-0-C₁₈ gave a hydrocarbon tail layer thickness of around 21 Å. This is consistent with the length of the fully extended hydrocarbon chain of the molecule (\sim 21 Å as calculated by

MMFF in vacuum) considering the uncertainty ranges associated with the slight tilt in the molecule at the corresponding surface pressures, as seen in the GIXD measurements (Table 2).

4. CONCLUSIONS

In terms of key monolayer packing and mechanical and crystallographic characteristics, the use of the "gemini without a spacer" motif in the surfactant headgroup has been of significant impact. Monolayers of C₁₈-0-C₁₈ are broadly comparable with those of simple fatty acids in terms of forming crystalline, close-packed structures that exhibit a tilted to untilted phase transition, as opposed to the disordered liquid films from Ace(n)-2-Ace(n) (n = 12, 18) comparators. The monolayers are also more stable than the liquid films at the air-water interface and transfer with better, albeit still flawed, efficiency onto solid substrates. The working hypothesis here is that the combination of greater structural headgroup rigidity with lower steric bulk of the headgroup is responsible for these differences in the monolayers. We also believe that this outcome may provide a more general molecular design criteria for synthesizing gemini surfactants that form rigid, stable, and crystalline monolayers at interfaces. However, subtle chemical structural details may be important here. While using Ace(n)-2-Ace(n) surfactants as comparator compounds appears reasonable, these compounds contain additional amine groups in their headgroups, and intermolecular interactions (through nitrogen lone pairs) associated with these groups might be particularly impactful in favoring the formation of liquid films. Further synthetic exploration of structures is needed to deconvolute this effect, though it may also provide an additional useful chemical structure factor for further tuning monolayer properties.

ASSOCIATED CONTENT

Supporting Information

The Supporting Information is available free of charge at https://pubs.acs.org/doi/10.1021/acs.langmuir.2c02462.

 1 H NMR spectrum, mass spectrum, powder X-ray diffraction pattern for purified C_{18} -0- C_{18} , comparison of BAM images for pure C_{18} -0- C_{18} and Ace(18)-2-Ace(18), AFM height-mode image for C_{18} -0- C_{18} deposited onto a solid substrate, GIXD contour plots for C_{18} -0- C_{18} at intermediate surface pressures, and a summary of GIXD data for pure C_{18} -0- C_{18} monolayer films at intermediate surface pressures (PDF)

AUTHOR INFORMATION

Corresponding Author

Matthew F. Paige – Department of Chemistry, University of Saskatchewan, Saskatoon, SK S7N 5C9, Canada;

orcid.org/0000-0002-5552-8123; Email: matthew.paige@usask.ca

Authors

Srikant Kumar Singh — Department of Chemistry, University of Saskatchewan, Saskatoon, SK S7N 5C9, Canada

Alfred Yeboah — Department of Chemistry, University of Saskatchewan, Saskatoon, SK S7N 5C9, Canada

Wei Bu — NSF's ChemMatCARS, Pritzker School of Molecular Engineering, University of Chicago, Chicago,

Illinois 60637, United States; oorcid.org/0000-0002-9996-3733

Pan Sun – NSF's ChemMatCARS, Pritzker School of Molecular Engineering, University of Chicago, Chicago, Illinois 60637, United States; orcid.org/0000-0002-6128-8656

Complete contact information is available at: https://pubs.acs.org/10.1021/acs.langmuir.2c02462

Notes

The authors declare no competing financial interest.

ACKNOWLEDGMENTS

S.S. thanks Dr. David Ci Yan for insightful discussions and help with designing the synthesis scheme for C_{18} -0- C_{18} . Financial support for this work has been provided by the Natural Sciences and Engineering Research Council, the Canadian Foundation for Innovation, and the University of Saskatchewan. NSF's ChemMatCARS Sector 15 is supported by the Divisions of Chemistry (CHE) and Materials Research (DMR), the National Science Foundation, under grant number NSF/CHE-1834750. Use of the Advanced Photon Source, an Office of Science User Facility operated for the U.S. Department of Energy (DOE), Office of Science by Argonne National Laboratory, was supported by the U.S. DOE under contract no. DE-AC02-06CH11357.

REFERENCES

- (1) Bhadani, A.; Misono, T.; Singh, S.; Sakai, K.; Sakai, H.; Abe, M. Structural Diversity, Physicochemical Properties and Application of Imidazolium Surfactants: Recent Advances. *Adv. Colloid Interface Sci.* **2016**, 231, 36–58.
- (2) Rosen, M. J. Gemini: A New Generation of Surfactants. J. Chemtech 1993, 30–30.
- (3) Holmberg, K. Novel Surfactants: Preparation Applications and Biodegradability, Revised and Expanded; CRC Press, 2003; Vol. 114.
- (4) Menger, F. M.; Keiper, J. S. Gemini Surfactants. *Angew. Chem. Int. Ed* **2000**, 39 (11), 1906–1920.
- (5) Behler, A.; Biermann, M.; Hill, K.; Raths, H.-C.; Victor, M.; Uphues, G.; Texter, J. In *Reactions and Synthesis in Surfactant Systems*; Texter, J., Ed.; Surfactant Science Series, v. 100; 2001; Industrial Surfactant Syntheses, pp 1–44
- (6) Wattebled, L.; Laschewsky, A. New Anionic Gemini Surfactant Based on EDTA Accessible by Convenient Synthesis. *Colloid Polym. Sci.* **2007**, 285 (12), 1387–1393.
- (7) Zana, R. Gemini Surfactants. In *Novel Surfactants*; CRC Press, 2003; pp 403-442.
- (8) Shukla, D.; Tyagi, V. Cationic Gemini Surfactants: A Review. *J. Oleo Sci.* **2006**, *55* (8), 381–390.
- (9) Pérez, L.; Pinazo, A.; Pons, R.; Infante, Mr. Gemini Surfactants from Natural Amino Acids. *Adv. Colloid Interface Sci.* **2014**, 205, 134–155
- (10) Huo, Q.; Leon, R.; Petroff, P. M.; Stucky, G. D. Mesostructure Design with Gemini Surfactants: Supercage Formation in a Three-Dimensional Hexagonal Array. *Science* **1995**, *268* (5215), 1324–1327.
- (11) Menger, F. M.; Mbadugha, B. N. A. Gemini Surfactants with a Disaccharide Spacer. J. Am. Chem. Soc. 2001, 123 (5), 875–885.
- (12) Zana, R.; Xia, J. Gemini Surfactants Synthesis, Interfacial and Solution-Phase Behavior, and Applications; Marcel Dekker: New York, 2004.
- (13) Menger, F. M.; Migulin, V. A. Synthesis and Properties of Multiarmed Geminis. J. Org. Chem. 1999, 64 (24), 8916–8921.
- (14) Zana, R.; Talmon, Y. Dependence of Aggregate Morphology on Structure of Dimeric Surfactants. *Nature* **1993**, *362* (6417), 228–230.
- (15) Sharma, R.; Kamal, A.; Abdinejad, M.; Mahajan, R. K.; Kraatz, H.-B. Advances in the Synthesis, Molecular Architectures and

- Potential Applications of Gemini Surfactants. Adv. Colloid Interface Sci. 2017, 248, 35–68.
- (16) Sakai, K.; Sakai, H.; Abe, M. Recent Advances in Gemini Surfactants: Oleic Acid-Based Gemini Surfactants and Polymerizable Gemini Surfactants. *J. Oleo Sci.* **2011**, *60* (4), 159–163.
- (17) Rosen, M. J.; Tracy, D. J. Gemini Surfactants. J. Surfactants Deterg 1998, 1 (4), 547–554.
- (18) Kirby, A. J.; Camilleri, P.; Engberts, J. B. F. N.; Feiters, M. C.; Nolte, R. J. M.; Söderman, O.; Bergsma, M.; Bell, P. C.; Fielden, M. L.; García Rodríguez, C. L.; Guédat, P.; Kremer, A.; McGregor, C.; Perrin, C.; Ronsin, G.; van Eijk, M. C. P. Gemini Surfactants: New Synthetic Vectors for Gene Transfection. *Angew. Chem. Int. Ed* 2003, 42 (13), 1448–1457.
- (19) In, M.; Zana, R. Phase Behavior of Gemini Surfactants. J. Dispers. Sci. Technol. 2007, 28 (1), 143–154.
- (20) Han, Y.; Wang, Y. Aggregation Behavior of Gemini Surfactants and Their Interaction with Macromolecules in Aqueous Solution. *Phys. Chem. Chem. Phys.* **2011**, *13* (6), 1939.
- (21) Hait, S. K.; Moulik, S. P. Gemini Surfactants: A Distinct Class of Self-Assembling Molecules. *Curr. Sci.* **2002**, 82 (9), 11.
- (22) Zana, R. Dimeric and Oligomeric Surfactants. Behavior at Interfaces and in Aqueous Solution: A Review. *Adv. Colloid Interface Sci.* **2002**, 97 (1–3), 205–253.
- (23) Lv, J.; Qiao, W.; Xiong, C. Synthesis and Surface Properties of a PH-Regulated and PH-Reversible Anionic Gemini Surfactant. *Langmuir* **2014**, *30* (28), 8258–8267.
- (24) Lv, J.; Qiao, W. Unusual PH-Regulated Surface Adsorption and Aggregation Behavior of a Series of Asymmetric Gemini Amino-Acid Surfactants. *Soft Matter* **2015**, *11* (13), 2577–2585.
- (25) Villa, C.; Baldassari, S.; Martino, D. F. C.; Spinella, A.; Caponetti, E. Green Synthesis, Molecular Characterization and Associative Behavior of Some Gemini Surfactants without a Spacer Group. *Materials* **2013**, *6* (4), 1506–1519.
- (26) Zana, R.; Benrraou, M.; Rueff, R. Alkanediyl-Alpha., Omega-Bis(Dimethylalkylammonium Bromide) Surfactants. 1. Effect of the Spacer Chain Length on the Critical Micelle Concentration and Micelle Ionization Degree. *Langmuir* 1991, 7 (6), 1072–1075.
- (27) Menger, F. M.; Keiper, J. S.; Azov, V. Gemini Surfactants with Acetylenic Spacers. *Langmuir* **2000**, *16* (5), 2062–2067.
- (28) Zana, R. Dimeric (Gemini) Surfactants: Effect of the Spacer Group on the Association Behavior in Aqueous Solution. *J. Colloid Interface Sci.* **2002**, 248 (2), 203–220.
- (29) Acharya, D. P.; Gutiérrez, J. M.; Aramaki, K.; Aratani, K.; Kunieda, H. Interfacial Properties and Foam Stability Effect of Novel Gemini-Type Surfactants in Aqueous Solutions. *J. Colloid Interface Sci.* **2005**, *291* (1), *236*–243.
- (30) Acharya, D. P.; Kunieda, H.; Shiba, Y.; Aratani, K. Phase and Rheological Behavior of Novel Gemini-Type Surfactant Systems. *J. Phys. Chem. B* **2004**, *108* (5), 1790–1797.
- (31) Sharma, S. C.; Shrestha, R. G.; Varade, D.; Aramaki, K. Rheological Behavior of Gemini-Type Surfactant/Alkanolamide/Water Systems. *Colloids Surf. Physicochem. Eng. Asp* **2007**, 305 (1–3), 83–88.
- (32) Rehman, J.; Araghi, H. Y.; He, A.; Paige, M. F. Morphology and Composition of Structured, Phase-Separated Behenic Acid—Perfluorotetradecanoic Acid Monolayer Films. *Langmuir* **2016**, 32 (21), 5341–5349.
- (33) Qaqish, S. E.; Paige, M. F. Rippled Domain Formation in Phase-Separated Mixed Langmuir—Blodgett Films. *Langmuir* **2008**, 24 (12), 6146–6153.
- (34) Malta, V.; Celotti, G.; Zannetti, R.; Martelli, A. F. Crystal Structure of the C Form of Stearic Acid. *J. Chem. Soc. B Phys. Org.* 1971, 548.
- (35) Lee, K. Y. C. Collapse Mechanisms of Langmuir Monolayers. *Annu. Rev. Phys. Chem.* **2008**, 59 (1), 771–791.
- (36) Petty, M. C. Langmuir-Blodgett Films; Cambridge University Press, 1996. DOI: 10.1017/CBO9780511622519.

- (37) Qaqish, S. E.; Paige, M. F. Mechanistic Insight into Domain Formation and Growth in a Phase-Separated Langmuir—Blodgett Monolayer. *Langmuir* **2007**, 23 (20), 10088–10094.
- (38) Brzozowska, A. M.; Duits, M. H. G.; Mugele, F. Stability of Stearic Acid Monolayers on Artificial Sea Water. *Colloids Surf. Physicochem. Eng. Asp* **2012**, 407, 38–48.
- (39) Eftaiha, A. F.; Paige, M. F. Phase-Separation of Mixed Surfactant Monolayers: A Comparison of Film Morphology at the Solid—Air and Liquid—Air Interfaces. *J. Colloid Interface Sci.* **2012**, 380 (1), 105–112.
- (40) Sah, B. K.; Das, K.; Kundu, S. PH-Dependent Structure, Pattern and Hysteresis Behaviour of Lipid (DMPA)-Protein (BSA) Monolayer Complex. *Colloids Surf. Physicochem. Eng. Asp* **2019**, *579*, 123663.
- (41) Tomoaia-Cotişel, M.; Zsako, J.; Chifu, E.; Quinn, P. J. Hysteresis in Compression-Expansion Cycles of Distearoylmonogalactosylglycerol Monolayers. *Chem. Phys. Lipids* **1989**, *50* (2), 127–133.
- (42) Sharma, S.; Radhakrishnan, T. P. Phospholipid–Fatty Acid Composite Monolayers: Analysis of the Pressure–Area Isotherms. *Thin Solid Films* **2001**, 382 (1–2), 246–256.
- (43) Reda, T.; Hermel, H.; Höltje, H.-D. Compression/Expansion Hysteresis of Poly(L-Glutamic Acid) Monolayers Spread at the Air/Water Interface. *Langmuir* **1996**, *12* (26), 6452–6458.
- (44) Sudheesh, S.; Ahmad, J.; Singh, G. S. Hysteresis of Isotherms of Mixed Monolayers of N -Octadecyl- N '-Phenylthiourea and Stearic Acid at Air/Water Interface. *ISRN Phys. Chem.* **2012**, 2012, 1–6.
- (45) Risović, D.; Frka, S.; Kozarac, Z. Application of Brewster Angle Microscopy and Fractal Analysis in Investigations of Compressibility of Langmuir Monolayers. *J. Chem. Phys.* **2011**, *134* (2), 024701.
- (46) Siegel, S.; Hoenig, D.; Vollhardt, D.; Moebius, D. Direct Observation of Three-Dimensional Transformation of Insoluble Monolayers. *J. Phys. Chem.* **1992**, *96* (20), 8157–8160.
- (47) Daear, W.; Mahadeo, M.; Prenner, E. J. Applications of Brewster Angle Microscopy from Biological Materials to Biological Systems. *Biochim. Biophys. Acta BBA Biomembr* **2017**, *1859* (10), 1749–1766.
- (48) Petrov, J. G.; Brezesinski, G.; Krasteva, N.; Möhwald, H. Langmuir Monolayers with Fluorinated Groups in the Hydrophilic Head: 2. Morphology and Molecular Structure of Trifluoroethyl Behenate and Ethyl Behenate Monolayers. *Langmuir* **2001**, *17* (15), 4581–4592.
- (49) Sowah-Kuma, D.; Rehman, J.; Yeboah, A.; Bu, W.; Yan, C.; Paige, M. F. Iron Binding in an Ethylenediaminetetracetic Acid-Based Gemini Surfactant Monolayer Film. *J. Surfactants Deterg* **2021**, *24* (6), 897–907.
- (50) Rehman, J.; Sowah-Kuma, D.; Stevens, A. L.; Bu, W.; Paige, M. F. Mixing Behavior in Binary Anionic Gemini Surfactant—Perfluorinated Fatty Acid Langmuir Monolayers. *Langmuir* **2017**, 33 (39), 10205—10215.
- (51) Rehman, J.; Sowah-Kuma, D.; Stevens, A. L.; Bu, W.; Paige, M. F. Immiscible Anionic Gemini Surfactant-Perfluorinated Fatty Acid Langmuir Monolayer Films. *Langmuir* **2019**, *35* (32), 10551–10560.
- (52) Als-Nielsen, J.; Jacquemain, D.; Kjaer, K.; Leveiller, F.; Lahav, M.; Leiserowitz, L. Principles and Applications of Grazing Incidence X-Ray and Neutron Scattering from Ordered Molecular Monolayers at the Air-Water Interface. *Phys. Rep* **1994**, 246 (5), 251–313.
- (53) Patterson, A. L. The Scherrer Formula for X-Ray Particle Size Determination. *Phys. Rev.* **1939**, *56* (10), 978–982.
- (54) Sowah-Kuma, D.; Fransishyn, K. M.; Cayabyab, C.; Martynowycz, M. W.; Kuzmenko, I.; Paige, M. F. Molecular-Level Structure and Packing in Phase-Separated Arachidic Acid—Perfluorotetradecanoic Acid Monolayer Films. *Langmuir* **2018**, *34* (36), 10673–10683.
- (55) Danauskas, S. M.; Li, D.; Meron, M.; Lin, B.; Lee, K. Y. C. Stochastic Fitting of Specular X-Ray Reflectivity Data Using *StochFit. J. Appl. Crystallogr.* **2008**, *41* (6), 1187–1193.

□ Recommended by ACS

Understanding the Hydration Thermodynamics of Cationic Quaternary Ammonium and Charge-Neutral Amine Surfactants

Himanshu Singh and Sumit Sharma

NOVEMBER 17, 2022

THE JOURNAL OF PHYSICAL CHEMISTRY B

READ 🗹

Interfacial Behavior of Modified Nicotinic Acid as Conventional/Gemini Surfactants

Ala'a F. Eftaiha, Matthew F. Paige, et al.

JULY 01, 2022

LANGMUIR

READ 🗹

Counterions under a Surface-Adsorbed Cationic Surfactant Monolayer: Structure and Thermodynamics

Eli Sloutskin, Moshe Deutsch, et al.

SEPTEMBER 28, 2022

LANGMUIR

READ 🗹

Exploration of the Adsorption Kinetics of Surfactants at the Water-Oil Interface via Grand-Canonical Molecular Dynamics Simulations

Xue-Dan Yang, Liang-Yin Chu, et al.

JANUARY 11, 2022

LANGMUIR

READ 🗹

Get More Suggestions >